

# Interface Reactions in LSMO–Metal Hybrid Structures

Nico Homonay,<sup>†</sup> Kerry J. ÓShea,<sup>‡</sup> Christian Eisenschmidt,<sup>†</sup> Martin Wahler,<sup>†</sup> Donald A. MacLaren,<sup>\*,‡</sup> and Georg Schmidt<sup>\*,†,§</sup>

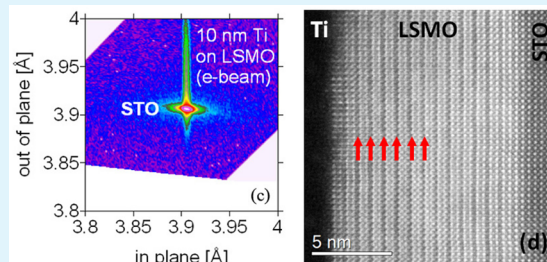
<sup>†</sup>Institut für Physik, Martin-Luther University Halle-Wittenberg, Von-Danckelmann-Platz 3 06120 Halle, Germany

<sup>‡</sup>SUPA, School of Physics and Astronomy, University of Glasgow, Glasgow G12 8QQ, United Kingdom

<sup>§</sup>Interdisziplinäres Zentrum für Materialwissenschaften, Martin-Luther University Halle-Wittenberg, Nanotechnikum Weinberg, Heinrich-Damerow-Straße 4 06120 Halle, Germany

**ABSTRACT:** Perovskites form a class of promising materials for the development of multifunctional devices but require reliable strategies for forming electrical contacts without compromising functionality. We explore the interactions of a range of metal contacts with ferromagnetic oxide  $\text{La}_{0.7}\text{Sr}_{0.3}\text{MnO}_3$  (LSMO) and discuss their impact on the magnetic, structural, and chemical properties of the oxide. Although the noble metals gold and silver have negligible impact, metals typically used as adhesion layers, such as titanium and chromium, drive substantial reduction of the oxide, impairing its performance. These effects can be suppressed by inserting a thin barrier layer, such as the conductive oxide  $\text{SrRuO}_3$ .

**KEYWORDS:** LSMO, LSMO–metal interfaces, complex oxide–metal interfaces, complex oxide electrical contacts, complex oxide degradation, LSMO oxygen deficiency



## I. INTRODUCTION

Advanced oxides are now the focus of intense research activity, driven by their numerous attractive properties for next generation microelectronics.<sup>1</sup> Of particular interest is ferromagnetic  $\text{La}_{0.7}\text{Sr}_{0.3}\text{MnO}$  (LSMO), which has a high Curie temperature<sup>2</sup> ( $\sim 370$  K), high spin polarization,<sup>3</sup> and colossal magnetoresistance, making it a promising candidate for room temperature spintronic applications<sup>4</sup> and spin pumping,<sup>5</sup> where the principal focus lies at the oxide–metal interface. Crucially, such metal–oxide hybrid devices rely on smooth interfaces, good electrical contact, and an absence of interfacial chemical reactions, because the functionality of oxides such as LSMO is known to be sensitive to changes in stoichiometry and strain.<sup>6</sup> For example, LSMO can undergo a phase change to a vacancy-ordered superlattice driven by either epitaxial strain<sup>7–13</sup> or contact with a reducing agent.<sup>14–17</sup> Thus, a comprehensive understanding of the effect of depositing metallic contacts onto perovskites is essential before functional metal–oxide hybrid devices can be realized. Here, we present a systematic study of the magnetic and structural effects of depositing metal contacts onto LSMO thin films. We find that the magnetization of  $>10$  nm thick oxide can be completely quenched after the deposition of just a few nanometers of a reducing metal. However, we can fully preserve the magnetic properties by exposing the LSMO to air prior to metallization or by inserting a suitable epitaxial conductive oxide. We thereby outline clear strategies toward the realization of multifunctional oxide devices.

## II. EXPERIMENTAL SECTION

Pulsed laser deposition (PLD)<sup>18</sup> was used for epitaxial growth of LSMO,  $\text{SrRuO}_3$  (SRO), and  $\text{SrTiO}_3$  (STO) using (100)-oriented STO substrates and stoichiometric polycrystalline targets. The PLD system employed a KrF excimer (248 nm) laser, and the growth was monitored *in situ* by high pressure reflection high energy electron diffraction (RHEED).<sup>19</sup> Ten nanometer and 20 nm thick LSMO films were deposited at laser fluencies of  $2\text{--}3 \text{ J/cm}^2$ , a repetition rate of 5 Hz, an  $\text{O}_2$  atmosphere of 0.2 mbar, and a substrate temperature of 700 °C. Previous experiments had shown that under these conditions LSMO films with correct stoichiometry and good magnetic properties can be grown.<sup>20</sup> Following deposition of the oxide layer(s), samples were transferred under UHV to an electron beam evaporation chamber for deposition of the metals.

Structural characterization was carried out using X-ray diffraction (XRD) and scanning transmission electron microscopy (STEM). XRD was performed on a BRUKER D8 diffractometer, and STEM was performed on a JEOL ARM 200cF microscope that is equipped with a cold field emission gun and operated at 200 kV. Cross-sectional samples for STEM were prepared on an FEI Nova Dualbeam Focused Ion Beam instrument. Electron energy loss spectroscopy (EELS) was conducted using a Gatan Quantum 965 spectrometer employing the Dual EELS<sup>21</sup> and spectrum imaging<sup>22</sup> methodologies, typically using a pixel step size of 0.5 Å and an acquisition time of 0.2 s per pixel to reduce spatial drift and beam damage. Principal component analysis (PCA) was used in some cases to isolate spectral features from the background and noise.<sup>23</sup>

**Received:** May 22, 2015

**Accepted:** September 24, 2015

**Published:** September 24, 2015



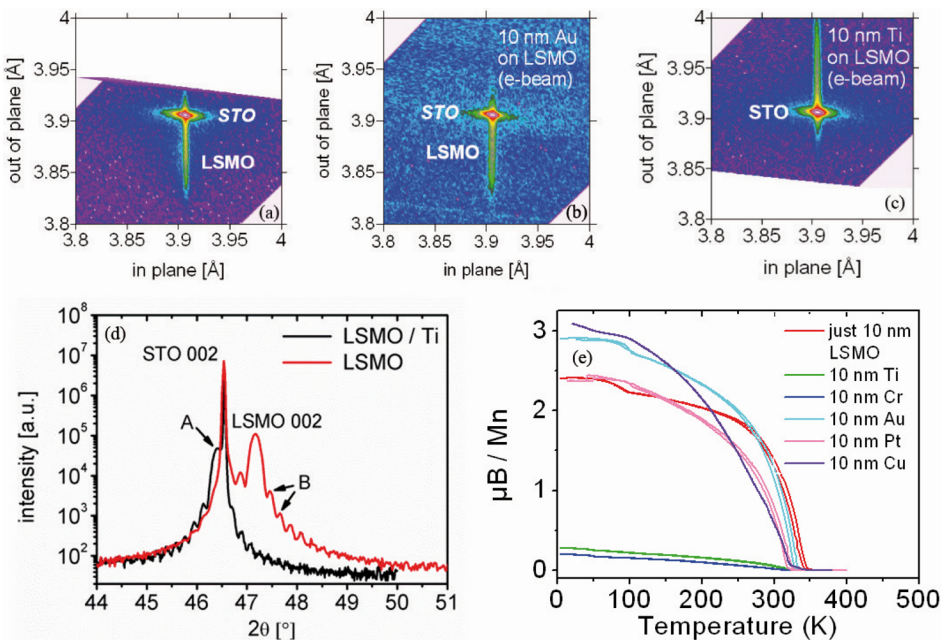


**Figure 1.** X-ray diffraction reciprocal space maps using the (002) Bragg reflection of LSMO (a) before and (b,c) after deposition of either 10 nm Au or 10 nm Ti. (d) A comparison of the intensity profiles more clearly shows a shift in peak position upon Ti deposition. (e) SQUID measurements indicate a reduction of LSMO magnetization upon deposition of Ti and Cr in particular, whereas Pt, Cu, and Au have less effect.

Magnetic characterization was performed using SQUID magnetometry with a Quantum Design, Incorporated, MPMS SQUID VSM, measuring from 380 K down to 4.2 K in a magnetic field of 20 Oe.

### III. RESULTS

XRD was used to determine the relaxation behavior and out-of-plane lattice constants by preparing reciprocal space maps around the (103) STO reflection, as summarized in Figure 1. For a single LSMO layer, shown in Figure 1a, the STO substrate peak is clearly visible with the LSMO peak corresponding to a perpendicular lattice constant of 3.859 nm. Although the deposition of a 10 nm thick Au layer had no impact on the lattice constants of the LSMO layer (Figure 1b), the deposition of a 10 nm thick Ti layer produced an entirely different result, as shown in Figure 1c and d. It can be seen from the XRD diffractogram of Figure 1d that the (002) reflection from LSMO/Ti has clearly shifted to lower angles (labeled “A” in Figure 1a), corresponding to a larger out-of-plane lattice constant. Although the in-plane lattice constant is unchanged, the lattice has apparently shifted from its original compressive strain to a tensed state with a lattice *c*-parameter of 3.956 nm. Shifting of the out-of-plane lattice constant has previously been reported for LSMO, resulting from an oxygen deficiency.<sup>24</sup> Despite this, the thickness fringes in Figure 1d, highlighted by the arrows at B, indicate very smooth interfaces. Similar changes in the LSMO out-of-plane lattice constant were observed following the deposition of both Cr and Ta capping layers (not shown here). However, the position of the LSMO peak was unchanged for noble metals, such as Ag, Pt, or Cu.

The temperature-dependent magnetization of the metallized LSMO films is indicated in Figure 1e. The isolated 10 nm thick LSMO layer (red curve in Figure 1e) had a Curie temperature of ~350 K and a magnetization of ~2.4  $\mu_B$ /Mn atom at 4.2 K, which is in good agreement with the best values seen in the literature<sup>25</sup> for a Sr content of 30%. Deposition of 10 nm of Ti or Cr, however, almost completely quenched the magnetization (Figure 1e, blue and green curves). The fact that the

magnetization is massively reduced while the Curie temperature for the remaining magnetization remains more or less unchanged indicates that what is observed is not just an overall deterioration of magnetic properties but a complete disappearance of ferromagnetism in most of the layer. For other less reactive materials, such as Au, Pt, Ag, and Cu, only minor modifications were observed and may well be attributed to experimental error or small sample-to-sample variations in the LSMO.

The structure of films was assessed on the atomic scale using STEM, and Figure 2a shows a low-magnification overview of the STO//LSMO(10 nm)/Au(10 nm) film with an atomic-resolved view of the interface provided in Figure 2b. As this is a high-angle annular dark field (HAADF) image, the contrast derives primarily from atomic number variations with the Au layer appearing brightest. It may be observed that the oxide/metal interface is atomically sharp, the LSMO is of very high crystalline quality, and there are no obvious structural changes up to the Au/oxide interface. The Au layer was polycrystalline, and lattice fringes are observed in the upper region of Figure 2b.

Conversely, the deposition of 10 nm of polycrystalline Ti drives a structural phase change in the LSMO, and the close-up view in Figure 2d imaged along a  $<100>$  substrate direction clearly shows the formation of a superlattice with cell-doubling along the film’s out-of-plane direction. (Note that Ti has a lower atomic number than Au and thus appears darker with respect to the LSMO.) The change in cell periodicity is more clearly observed in the HAADF image intensity trace shown in blue in Figure 2e, which also includes EELS data that are discussed below. A number of previous studies have discussed structural transitions in the  $\text{La}_{1-x}\text{Sr}_x\text{MnO}_{3-y}$  system, as a function of both the  $(\text{La},\text{Sr})$  content<sup>26</sup> and oxygen deficiencies,<sup>27–29</sup> the latter commonly producing vacancy-ordered superstructures. We have no evidence for a change in the  $(\text{La},\text{Sr})$  content that was inferred from the high Curie temperature of the as-deposited LSMO films. However, the

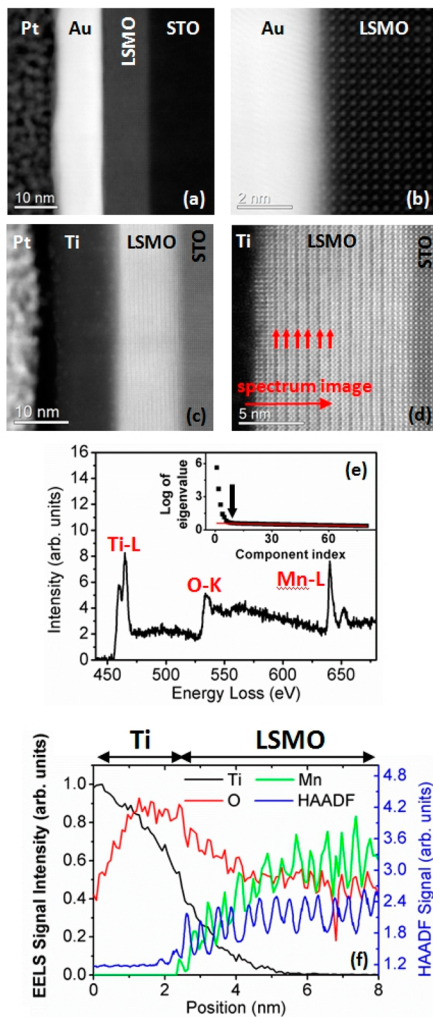


**Figure 2.** (a) Low magnification STEM image of the LSMO with Au cap. (b) High resolution view of the Au/LSMO boundary showing a high quality interface. (c) Low magnification STEM image of the Ti/LSMO film with a close-up view given in (d), where a complete phase transition can be observed. EELS data were acquired along the line indicated. (e) Typical background-subtracted EELS spectrum collected from the LSMO/Ti interface and spanning the Ti-L<sub>2,3</sub>, O-K, and Mn L<sub>2,3</sub> features after the application of principal component analysis. The (inset) scree plot indicates the spectra to be well-represented by 7 eigenfunctions (black arrow). (f) Integrated EELS intensities as a function of position across the interface indicate migration of O (red) into the Ti capping layer, thus providing an explanation for the phase transition.

HAADF image of Figure 2d strongly resembles those reported previously for brownmillerite systems, perhaps the most common oxygen vacancy-ordered structure to form for LSMO of this (La,Sr) content.<sup>12,30</sup> Brownmillerite structures, which do not support ferromagnetism, are a variant of the ABO<sub>3</sub> perovskite crystal, whereby half of the oxygen atoms have been removed from alternate BO<sub>2</sub> layers. This generates a stacking sequence of the form AO-BO<sub>2</sub>-AO-BO-AO, and the unit cell alternates between oxygen octahedra and oxygen tetrahedra centered on the B cation sites. At least 5 distinct variants of the brownmillerite structure have been described for La<sub>0.7</sub>Sr<sub>0.3</sub>MnO<sub>2.5</sub>, differing in the sense of rotation of the oxygen tetrahedra, although the HAADF imaging presented here cannot readily discriminate between these phases as the image contrast is dominated by heavier atoms whose positions may

not vary substantially. We measure the out-of-plane lattice parameter to be  $16.5 \pm 0.4$  Å, which is in excellent agreement with that found elsewhere.<sup>14</sup> The dark planes in Figure 2d coincide with the MnO<sub>2</sub> planes of the LSMO, indicating a deficiency in either manganese or oxygen. EELS data were subsequently recorded to investigate the location of oxygen in the film, and the results are presented in the lower panels of Figure 2. Figure 2e shows a typical EEL spectrum of the Ti/LSMO interface after removal of plural scattering effects and PCA analysis, containing the Ti L<sub>2,3</sub> edge, O K edge, and the Mn L<sub>2,3</sub> edge. Seven PCA eigenfunctions were deemed significant for analysis on the basis of the (inset) scree plot, which has an abrupt gradient change that separates statistically significant information from uncorrelated noise.<sup>23</sup> Figure 2f then plots the variation of the Ti L<sub>2,3</sub> (black), Mn L<sub>2,3</sub> (green), and O K (red) signals across the LSMO-Ti boundary. The HAADF signal intensity (blue) is also given to aid comparison with the STEM images. It can immediately be seen that the dark planes in the HAADF image coincide with peaks in the Mn signal and thus correspond to the MnO<sub>2</sub> planes of the original perovskite. The oxygen signal is more diffuse but extends a significant distance into the Ti layer, decaying at a considerably slower rate than the Mn signal, thus indicating that the Ti acted as an oxygen getter and has oxidized. The Ti L<sub>2,3</sub> ELNES spectrum is consistent with that of a TiO<sub>x</sub> phase, comprising two main broad L<sub>3</sub> and L<sub>2</sub> white lines.<sup>31</sup> A small degree of intermixing is apparent from the overlap of Ti and Mn signals but is ascribed to surface roughness. A comparison of the oxygen signal levels of the STO and brownmillerite LSMO regions indicates a decrease in oxygen in the LSMO brownmillerite phase (see below). Oxygen vacancies are typically compensated by a reduction of the Mn<sup>4+</sup> content to retain charge neutrality, which accounts for the loss of magnetization found in the LSMO here.<sup>32</sup>

EELS fine structures are plotted in Figure 3. The oxygen K near-edge fine structure in the EELS spectrum shows significant changes when the Mn oxidation state is modified, and three main features can be identified in Figure 3a in good agreement

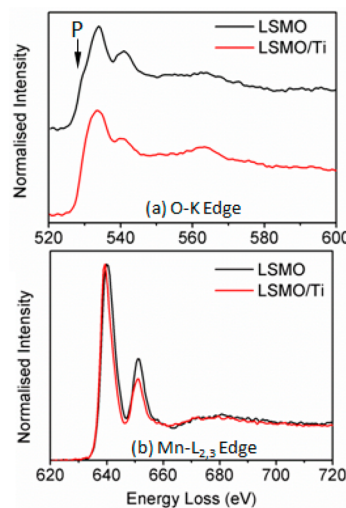


**Figure 3.** (a) Background-subtracted EELS spectra of the O K edge in the pristine LSMO film (black) and vacancy ordered phase (red). The pre-edge peak indicated by P is no longer discernible in the brownmillerite phase. (b) The Mn L<sub>2,3</sub> edge has an increased L<sub>3</sub>/L<sub>2</sub> peak intensity ratio in the vacancy ordered LSMO (red), consistent with a lowering of the Mn valence.

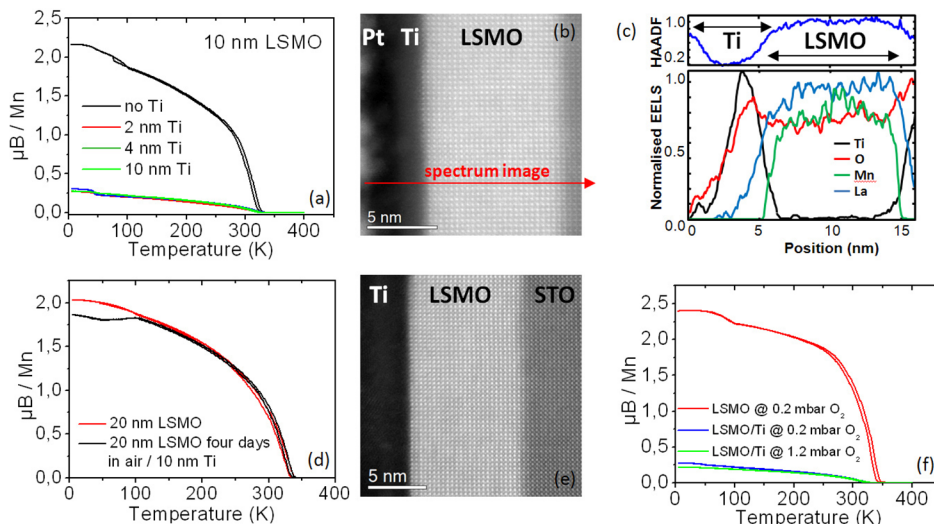


**Figure 4.** (a) SQUID measurements of Ti capping layers of different thicknesses. (b) STEM image of an LSMO film with a 2 nm thick Ti cap. (c) Corresponding EELS intensity profiles of Ti, O, Mn, and La signals across the Ti/LSMO stack, showing oxygen depletion in the LSMO and complementary oxidation of the Ti layer. Signals are normalized to their maximal values to aid comparisons. The locations of data acquisition are indicated approximately in the STEM image and by the HAADF data at the top of the plot. (d) Exposing the LSMO to air for 4 days prior to Ti deposition preserved the magnetic properties and (e) preserved the apparent crystal structure observed in STEM. (f) Changing the oxygen pressure during cooling of the LSMO film after deposition had no effect on the Ti-capped LSMO.

with previous observations:<sup>33</sup> a prepeak shoulder immediately at the onset (indicated by P in Figure 3a), a main peak at  $\sim$ 535 eV, and a third peak around 540 eV. A prepeak shoulder also occurs in other manganese oxide spectra, where it arises from excitation to an occupied orbital with a hybridized Mn 3d contribution<sup>34</sup> and is known to be sensitive to Mn d-band occupancy. We interpret the loss of the prepeak in the vacancy ordered LSMO film (red curve in Figure 3a) in comparison with that of bulk, uncompromised LSMO to indicate a similar reduction of the Mn valence.<sup>33</sup> Additionally, the “white line ratio” of the Mn L<sub>3</sub>/L<sub>2</sub> peaks (i.e., the ratio of L<sub>3</sub> to L<sub>2</sub> integrated intensities) is a well-established measure of transition metal valency and will generally increase with Mn chemical reduction.<sup>35</sup> A comparison of the Mn L<sub>2,3</sub> edge for pristine LSMO and the reconstructed film is given in Figure 3b, where an increase in the L<sub>3</sub>/L<sub>2</sub> peak ratio can be observed, thus confirming a reduction in Mn oxidation state. Together, the data are consistent with a chemical reduction of the Mn and consequent change in bonding environment through the creation of oxygen vacancies.

Given the technological relevance of Ti as a typical adhesion layer for noble metal electrical contacts,<sup>36</sup> we explored the thickness-dependence in more detail. Figure 4a illustrates the effect of varying the thickness of the Ti layer on LSMO. Interestingly, complete quenching of the LSMO magnetization occurs with the deposition of just  $\sim$ 2 nm of Ti, even though the crystal structure appears intact, as illustrated by the STEM image in Figure 4b. Again, the Ti L<sub>2,3</sub> ELNES spectrum is consistent with that of a TiO<sub>x</sub> phase with a similar appearance to that given in Figure 2e. Figure 4c presents EELS profiles of the Ti L<sub>2,3</sub>, O K, Mn L<sub>2,3</sub>, and La M<sub>4,5</sub> signals across the LSMO layer after deposition of  $\sim$ 2 nm of Ti. It may be observed that there is a significant oxygen signal throughout the Ti layer deposited onto the LSMO, whereas the LSMO layer itself is significantly deficient in oxygen with respect to the STO at the far right of the plot. The titanium oxide appears largely amorphous. To assess the oxygen deficiency, we measure the L<sub>3</sub>/L<sub>2</sub> intensity ratio using the methodology of Schmid and

Mader,<sup>37</sup> which corresponds roughly to a Mn valence of 4 (ignoring more subtle variations in the white line ratio that depend on the local bonding environment). For oxygen-deficient LSMO (i.e., La<sub>1-x</sub>Sr<sub>x</sub>MnO<sub>3-y</sub>), this yields  $y \leq 0.34$ , which is equivalent to approximately 11 at. % of the oxygen content,<sup>38</sup> suggesting that a relatively high density of oxygen vacancies can be supported prior to reconstruction.

In cases where the sequential deposition of oxide then metal is not possible without a vacuum break, the oxide film will be exposed to air for a period of time. Immediate deposition of Ti after a vacuum break has a similar deleterious effect on the LSMO as before. However, when the samples were held in air for 4 days, the magnetic properties of the LSMO were preserved after Ti deposition, as indicated in Figure 4d. The small decrease in magnetization below 105 K is due to a slight difference in cooling field and is unrelated to the metallization. At the structural phase transition in the STO substrate that occurs at this temperature, the magnetization and anisotropy of the LSMO changes slightly. Depending on the external field, the LSMO will either remain saturated or will shift slightly off-axis with respect to the field and thus no longer be detected by the magnetometer; the latter manifests as a small decrease in magnetization.

To determine whether the observed preservation of magnetization in Figure 4d could be ascribed to oxidation of the LSMO film in atmosphere, we subsequently increased the oxygen pressure from 0.2 to 1.2 bar during the cooling stage of the growth so that the sample would be exposed to oxygen while still hot and thereby react faster. However, the magnetization was still quenched by the deposition of Ti, as illustrated in Figure 4f, irrespective of the oxygen overpressure. This suggests that the as-grown films are stoichiometric (which one would surmise from their initially good magnetization) and that the four-day-long exposure to atmospheric conditions must instead diminish the rate of oxygen loss once the film is coated with Ti. It is therefore possible that adventitious contamination formed a thin barrier between Ti and LSMO, slowing oxygen migration and thus slowing the resulting redox reaction. No

such barrier was evident in STEM, although we cannot exclude the possible presence of a few monolayers of organic contamination. Indeed, although the crystal structure appeared intact in STEM imaging (see Figure 4e) after 4 days' exposure to the atmosphere, it was considerably less robust to electron dose in the microscope, and underwent a phase transition during data acquisition similar to that observed elsewhere.<sup>39</sup> This suggests that the oxygen content of the film had again been reduced by the Ti layer but not sufficient to impair either the magnetization or the apparent structure, i.e., that oxygen migration had been slowed but not halted. Although a systematic study was not conducted, we found that the LSMO still decomposed to a brownmillerite phase several months after Ti deposition onto the air-exposed LSMO. These results indicate the importance of understanding the kinetics and resulting time scales of the interfacial reactions that we observe: materials that appear initially uncompromised by metallization may subsequently degrade.

We now turn to strategies for minimizing the oxygen gettering effects of Ti and related adhesion layers. For many applications, the insertion of an epitaxial oxide between the LSMO and the metallic contact may be sufficient. If, for example, the metal is predominantly required to make ohmic contact to the LSMO layer, then one might use a thin SRO interlayer, which is highly conductive and nonmagnetic down to 150 K.<sup>40</sup> Conversely, an insulating STO interlayer may be used in cases where the metal is used purely as a mask for dry etching and electrical conductivity is not required. STO forms a convenient, readily deposited, and well-lattice-matched layer upon which the epitaxial growth of both Pt and Cu has previously been reported.<sup>41</sup> Irrespective of the application, it is desirable to keep the insertion layer thickness to a minimum, and we therefore compared the performance of 1, 4, and 10 nm thick layers of SRO and STO sandwiched between LSMO and Ti. The thicknesses are the nominal thicknesses according to deposition rate for stoichiometric material. They were also verified by X-ray reflectometry. For the thinnest layers, the X-ray reflectometry data may be subject to an error of  $\pm 0.5$  nm.

Figure 5a shows, from left to right, a series of reciprocal space maps for an LSMO layer without any protection layer and with SRO protective interlayers of increasing thickness. SQUID measurements (shown in Figure 5b) illustrate that a 1 nm SRO interlayer was insufficient to protect the LSMO, but that insertion of a 4 nm thick SRO layer preserved the magnetic moment of  $2.75 \mu_B/\text{Mn}$  atom, with XRD showing no change in the lattice constant, as observed in Figure 5a. Note that the kink in the SQUID curves at 150 K for SRO thicknesses of 4 nm and above is caused by the SRO layer itself, which is ferromagnetic below this temperature.<sup>36</sup> A similar pattern was observed for an STO interlayer, where 4 nm was sufficient to restore the magnetic properties of the LSMO, as illustrated by the SQUID measurements in Figure 5c. A STEM image summary of the LSMO/SRO/Ti film is given in Figure 6 for (a) a nominally 1 nm thick SRO interlayer and (b) a nominally 4 nm thick interlayer of SRO. Corresponding EELS profiles are given below and illustrate the Ti L<sub>2,3</sub>, O K, Mn L<sub>2,3</sub>, and La M<sub>4,5</sub> edge signal intensities across the stack. It is clear that for a 1 nm thick SRO interlayer, the gettering effect of the Ti significantly altered the SRO crystal structure, driving it to an amorphous state. The crystal degradation continues past the LSMO interface, so that the LSMO is again oxygen deficient, as confirmed by EELS. Conversely, only the lower  $\sim 2$  nm of the nominal 4 nm thick SRO film (Figure 6b) appeared structurally

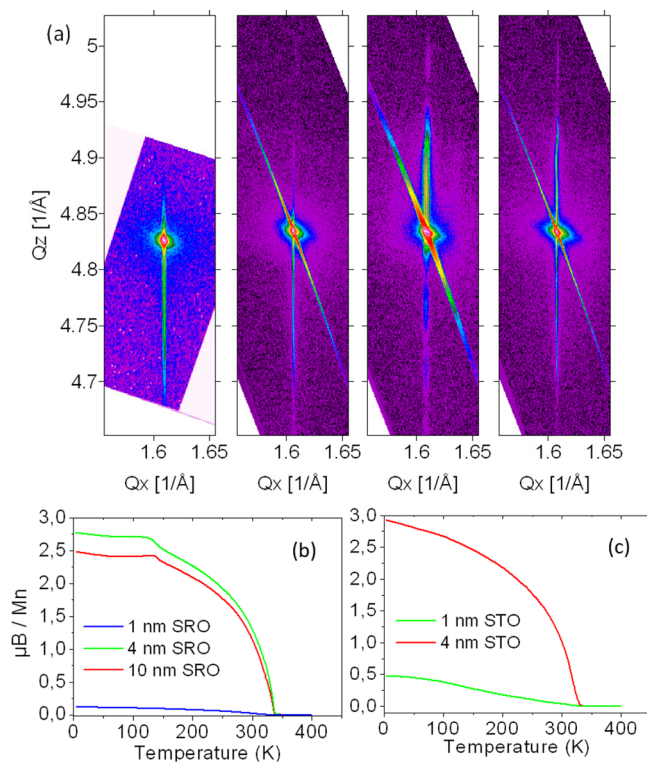


**Figure 5.** (a) A series of X-ray diffraction reciprocal space maps for LSMO/SRO/Ti stacks, where the SRO thickness ranges from 0 to 10 nm (left to right: 0, 1, 4, and 10 nm). SQUID measurements of LSMO films with different thicknesses of (b) an SRO interlayer and (c) an STO interlayer indicate that a 4 nm insertion layer is sufficient to prevent the quenching of magnetization whereas 1 nm thick layers are not.

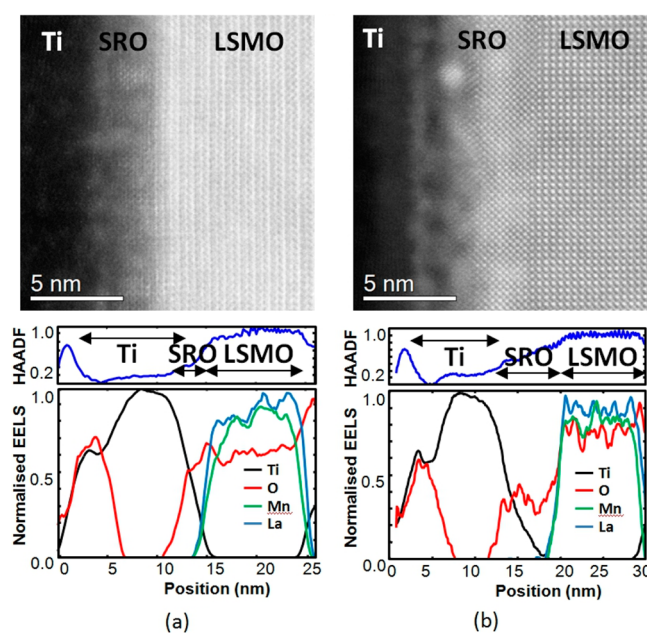


**Figure 6.** STEM image (top) and corresponding EELS profiles (bottom) for an SRO interlayer thickness of (a) 1 nm and (b) 4 nm. Signals are normalized to their maximal values to aid comparisons. The locations of data acquisition are indicated by the HAADF data at the top of the plot. The LSMO structure has drastically changed to a vacancy ordered state for just 1 nm of SRO, but 4 nm is sufficient to protect the LSMO, which remains intact.

intact. Note that the SRO layer thicknesses were determined by observation of X-ray reflectometry oscillations; in both STEM images, the apparent layer thickness is greater because of the diffuse nature of the intermixed region and surface roughness of the as-deposited SRO. In the case of the nominal 1 nm film, there is an ~2.5 nm thick oxygenated layer between the LSMO and unoxidized Ti that contains both titanium oxide and the amorphous decomposition products of SRO. In the case of the nominal 4 nm film, crystallinity (but reduced O content) is retained within the first ~2 nm, but the amorphous oxide extends a further ~5 nm into the Ti. Consequently, the LSMO crystal structure was preserved, and the thicker SRO film acted as an effective barrier to the Ti.

## IV. CONCLUSIONS

It is concluded that direct deposition of reducing metals, such as Ti or Cr, onto functional oxides should be avoided. In cases where LSMO layers in a similar configuration still show the original physical properties, the interface most likely contains a passivating contamination caused by prolonged exposure to atmospheric conditions. If reactive metals are required as adhesion layers for electrical contacts, then the insertion of a suitable epitaxial oxide, such as SrRuO<sub>3</sub>, can prevent degradation of the performance of La<sub>0.7</sub>Sr<sub>0.3</sub>MnO<sub>3</sub>. If a mask is required for subsequent lithographic purposes, then the deposition of Pt appears to be the most viable method, as it did not degrade the magnetic properties of the LSMO. These results provide valuable insight into the effects of metal contacting and ultimately enhance our understanding toward the development of uncompromised functional oxide devices.

## AUTHOR INFORMATION

### Corresponding Authors

\*E-mail: [georg.schmidt@physik.uni-halle.de](mailto:georg.schmidt@physik.uni-halle.de).

\*E-mail: [dmaclaren@physics.org](mailto:dmaclaren@physics.org).

### Notes

The authors declare no competing financial interest.

## ACKNOWLEDGMENTS

This work was funded by the EC's seventh Framework Program project "IFOX" (NMP3-LA-2010 246102), Engineering and Physical Sciences Research Council of the UK (EP/I00419X/1), and DFG in the SFB 762. We thank Jo Verbeeck from University of Antwerpen for fruitful discussion and support.

## REFERENCES

- (1) Haghiri-Gosnet, A. M.; Renard, J. P. CMR Manganites: Physics, Thin Films and Devices. *J. Phys. D: Appl. Phys.* **2003**, *36*, R127–R150.
- (2) Jonker, G. H.; van Santen, J. H. Ferromagnetic Compounds of Manganese with Perovskite Structure. *Physica* **1950**, *16*, 337–349.
- (3) Park, J. H.; Vescovo, E.; Kim, H. J.; Kwon, C.; Ramesh, R.; Venkatesan, T. Direct Evidence for a Half-Metallic Ferromagnet. *Nature* **1998**, *392*, 794–796.
- (4) Bowen, M.; Bibes, M.; Barthélémy, A.; Contour, J. P.; Anane, A.; Lemaitre, Y.; Fert, A. Nearly Total Spin Polarization in La<sub>2</sub>/3Sr<sub>1</sub>/3MnO<sub>3</sub> from Tunneling Experiments. *Appl. Phys. Lett.* **2003**, *82*, 233–235.
- (5) Ando, K.; Takahashi, S.; Ieda, J.; Kajiwara, Y.; Nakayama, H.; Yoshino, T.; Harii, K.; Fujikawa, Y.; Matsuo, M.; Maekawa, S.; Saitoh, E. Inverse Spin-Hall Effect Induced by Spin Pumping in Metallic System. *J. Appl. Phys.* **2011**, *109*, 103913.
- (6) Schumacher, D.; Steffen, A.; Voigt, J.; Schubert, J.; Brückel, T.; Ambaye, H.; Lauter, V. Inducing exchange bias in La<sub>0.67</sub>Sr<sub>0.33</sub>MnO<sub>3-δ</sub>/SrTiO<sub>3</sub> thin films by strain and oxygen deficiency. *Phys. Rev. B: Condens. Matter Mater. Phys.* **2013**, *88*, 144427.
- (7) Gazquez, J.; Bose, S.; Sharma, M.; Torija, M. A.; Pennycook, S. J.; Leighton, C.; Varela, M. Lattice Mismatch Accommodation via Oxygen Vacancy Ordering in Epitaxial La<sub>0.5</sub>Sr<sub>0.5</sub>CoO<sub>3-δ</sub> Thin Films. *APL Mater.* **2013**, *1*, 012105.
- (8) Pennycook, S.; Zhou, H.; Chisholm, M. F.; Borisevich, A. Y.; Varela, M.; Gazquez, J.; Pennycook, T. J.; Narayan, J. Misfit Accommodation in Oxide Thin Film Heterostructures. *Acta Mater.* **2013**, *61*, 2725–2733.
- (9) Torija, M.; Sharma, M.; Fitzsimmons, M. R.; Varela, M.; Leighton, C. Epitaxial La<sub>0.5</sub>Sr<sub>0.5</sub>CoO<sub>3</sub> Thin Films: Structure, Magnetism and Transport. *J. Appl. Phys.* **2008**, *104*, 023901.
- (10) Chen, Z. Q.; Cvelbar, U.; Mozetic, M.; He, J. Q.; Sunkara, M. K. Long-Range Ordering of Oxygen-Vacancy Planes in α-Fe<sub>2</sub>O<sub>3</sub> Nanowires and Nanobelts. *Chem. Mater.* **2008**, *20*, 3224–3228.
- (11) Kim, Y. M.; He, J.; Biegalski, M.; Ambaye, H.; Lauter, V.; Christen, H. M.; Pantelides, S. T.; Pennycook, S. J.; Kalinin, S. V.; Borisevich, A. Probing Oxygen Vacancy Concentration and Homogeneity in Solid-Oxide Fuel-Cell Cathode Materials on the Subunit-Cell Level. *Nat. Mater.* **2012**, *11*, 888–894.
- (12) Rossell, M. D.; Lebedev, O. I.; Van Tendeloo, G.; Hayashi, N.; Terashima, T.; Takano, M. Structure of Epitaxial Ca<sub>2</sub>Fe<sub>2</sub>O<sub>5</sub> Films Deposited on Different Perovskite-Type Substrates. *J. Appl. Phys.* **2004**, *95*, 5145–5152.
- (13) Parsons, T. G.; D'Hondt, H.; Hadermann, J.; Hayward, M. The Synthesis and Structural Characterization of La<sub>1-x</sub>A<sub>x</sub>MnO<sub>2.5</sub> (A = Ba, Sr, Ca) Phases – Mapping the Variants of the Brownmillerite Structure. *Chem. Mater.* **2009**, *21*, 5527–5538.
- (14) Ferguson, J. D.; Kim, Y.; Kourkoutis, L. F.; Vodnick, A.; Woll, A. R.; Muller, D. A.; Brock, J. D. Epitaxial Oxygen Getter for a Brownmillerite Phase Transformation in Manganite Films. *Adv. Mater.* **2011**, *23*, 1226–1230.
- (15) Brivio, S.; Magen, C.; Sidorenko, A.; Petti, D.; Cantoni, M.; Finazzi, M.; Cicacci, F.; Renzi, R.; Varela, M.; Picozzi, S.; Bertacco, R. Effects of Au Nanoparticles on the Magnetic and Transport Properties of La<sub>0.67</sub>Sr<sub>0.33</sub>MnO<sub>3</sub> Ultrathin Layers. *Phys. Rev. B: Condens. Matter Mater. Phys.* **2010**, *81*, 094410.
- (16) Casey, P. S.; Barker, D.; Hayward, M. A. Charge and Structural Ordering in the Brownmillerite Phases: La<sub>1-x</sub>Sr<sub>x</sub>MnO<sub>2.5</sub> (0.2 < x < 0.4). *J. Solid State Chem.* **2006**, *179*, 1375–1382.
- (17) Klie, R. F.; Ito, Y.; Stemmer, S.; Browning, N. S. Observation of Oxygen Vacancy Ordering and Segregation in Perovskite Oxides. *Ultramicroscopy* **2001**, *86*, 289–302.
- (18) Willmott, P. R.; Huber, J. R. Pulsed Laser Vaporization and Deposition. *Rev. Mod. Phys.* **2000**, *72*, 315–328.
- (19) Neave, J. H.; Joyce, B. A.; Dobson, P. J.; Norton, N. Dynamics of Film Growth of GaAs by MBE from RHEED Observations. *Appl. Phys. A: Solids Surf.* **1983**, *31*, 1–8.
- (20) Wahler, M.; Büttner, B.; Blaschek, H. H.; Homonnay, N.; Wid, O.; O'Shea, K. J.; McGrouther, D.; MacLaren, D. A.; Schmidt, G. Controlling Magnetic Anisotropy in La<sub>0.7</sub>Sr<sub>0.3</sub>MnO<sub>3</sub> Nanostructures. *Appl. Phys. Lett.* **2014**, *104*, 052408.
- (21) Scott, J.; Thomas, P. J.; MacKenzie, M.; McFadzean, S.; Wilbrink, J.; Craven, A. J.; Nicholson, W. A. P. Near-Simultaneous Dual Energy Range EELS Spectrum Imaging. *Ultramicroscopy* **2008**, *108*, 1586–1594.
- (22) Hunt, J. A.; Williams, D. B. Electron Energy-Loss Spectroscopy-Imaging. *Ultramicroscopy* **1991**, *38*, 47–73.
- (23) Bosman, M.; Watanabe, M.; Alexander, D. T. L.; Keast, V. J. Mapping Chemical and Bonding Information Using Multivariate Analysis of Electron Energy-Loss Spectrum Images. *Ultramicroscopy* **2006**, *106*, 1024–1032.
- (24) Li, J.; Liu, J. M.; Li, H. P.; Fang, H. C.; Ong, C. K. Magnetoresistance in Oxygen Deficient La<sub>0.75</sub>Sr<sub>0.25</sub>MnO<sub>3-δ</sub> Thin Films Prepared by Pulsed Laser Deposition. *J. Magn. Magn. Mater.* **1999**, *202*, 285–291.
- (25) Boschker, H.; Huijben, M.; Vailionis, A.; Verbeeck, J.; van Aert, S.; Luysberg, M.; Bals, S.; van Tendeloo, G.; Houwman, E. P.; Koster,

- G.; Blank, D. H. A.; Rijnders, G. Optimized Fabrication of High-Quality  $\text{La}_{0.67}\text{Sr}_{0.33}\text{MnO}_3$  Thin Films Considering All Essential Characteristics. *J. Phys. D: Appl. Phys.* **2011**, *44*, 205001.
- (26) Hemberger, J.; Krimmel, A.; Kurz, T.; Krug von Nidda, H.-A.; Ivanov, V. Y.; Mukhin, A. A.; Balbashov, A. M.; Loidl, A. Structural, Magnetic, and Electrical Properties of Single-Crystalline  $\text{La}_{1-x}\text{Sr}_x\text{MnO}_3$ . *Phys. Rev. B: Condens. Matter Mater. Phys.* **2002**, *66*, 094410.
- (27) Casey, P. S.; Barker, D.; Hayward, M. A. Charge and Structural Ordering in the Brownmillerite Phases:  $\text{La}_{1-x}\text{Sr}_x\text{MnO}_{2.5}$  ( $0.2 < x < 0.4$ ). *J. Solid State Chem.* **2006**, *179*, 1375–1382.
- (28) Parsons, T. G.; D'Hondt, H.; Hadermann, J.; Hayward, M. A. Synthesis and Structural Characterization of  $\text{La}_{1-x}\text{A}_x\text{MnO}_{2.5}$  ( $\text{A} = \text{Ba}, \text{Sr}, \text{Ca}$ ) Phases: Mapping the Variants of the Brownmillerite Structure. *Chem. Mater.* **2009**, *21*, 5527–5538.
- (29) Dixon, E.; Hadermann, J.; Hayward, M. A. The Synthesis and Complex Anion-Vacancy Ordered Structure of  $\text{La}_{0.33}\text{Sr}_{0.67}\text{MnO}_{2.42}$ . *J. Solid State Chem.* **2011**, *184*, 1791–1799.
- (30) Klenov, D. O.; Donner, W.; Foran, B.; Stemmer, S. Impact of stress on oxygen vacancy ordering in epitaxial (La 0.5 Sr 0.5) CoO 3- $\delta$  thin films. *Appl. Phys. Lett.* **2003**, *82*, 3427–3429.
- (31) Stoyanov, E.; Langenhorst, F.; Steinle-Neumann, G. The Effect of Valence State and Site Geometry on Ti L-3, L-2 and OK Electron Energy-Loss Spectra of  $\text{Ti}_{x}\text{O}_y$  Phases. *Am. Mineral.* **2007**, *92*, 577–586.
- (32) Cauro, R.; Gilabert, A.; Contour, J. P.; Lyonnet, R.; Medici, M. G.; Grenet, J. C.; Leighton, C.; Schuller, I. K. Persistent and Transient Photoconductivity in Oxygen-Deficient  $\text{La}_{2/3}\text{Sr}_{1/3}\text{MnO}_{3-\delta}$  Thin Films. *Phys. Rev. B: Condens. Matter Mater. Phys.* **2001**, *63*, 174423.
- (33) Varela, M.; Oxley, M. P.; Luo, W.; Tao, J.; Watanabe, M.; Lupini, A. R.; Pantelides, S. T.; Pennycook, S. J. Atomic-Resolution Imaging of Oxidation States in Manganites. *Phys. Rev. B: Condens. Matter Mater. Phys.* **2009**, *79*, 085117.
- (34) Kurata, H.; Colliex, C. Electron-Energy-Loss Core-Edge Structures in Manganese Oxides. *Phys. Rev. B: Condens. Matter Mater. Phys.* **1993**, *48*, 2102–2108.
- (35) Li, Z. P.; Bosman, M.; Yang, Z.; Ren, P.; Wang, L.; Cao, L.; Yu, X. J.; Ke, C.; Breese, M. B. H.; Rusydi, A.; Zhu, W. G.; Dong, Z. L.; Foo, Y. L. Interface and Surface Cation Stoichiometry Modified by Oxygen Vacancies in Epitaxial Manganite Films. *Adv. Funct. Mater.* **2012**, *22*, 4312–4321.
- (36) Yang, J. J.; Strachan, J. P.; Xia, Q. F.; Ohlberg, D. A. A.; Kuekes, P. J.; Kelley, R. D.; Stickle, W. F.; Stewart, D. R.; Medeiros-Ribeiro, G.; Williams, R. S. Diffusion of Adhesion Layer Metals Controls Nanoscale Memristive Switching. *Adv. Mater.* **2010**, *22*, 4034–4038.
- (37) Schmid, H. K.; Mader, W. Oxidation States of Mn and Fe in Various Compound Oxide Systems. *Micron* **2006**, *37*, 426–432.
- (38) Wang, Z. L.; Yin, J. S.; Jiang, Y. D. EELS Analysis of Cation Valence States and Oxygen Vacancies in Magnetic Oxides. *Micron* **2000**, *31*, 571–580.
- (39) Yao, L. D.; Majumdar, S.; Äkäslompolo, L.; Inkinen, S.; Qin, Q. H.; van Dijken, S. Electron-Beam-Induced Perovskite–Brownmillerite–Perovskite Structural Phase Transitions in Epitaxial  $\text{La}_{2/3}\text{Sr}_{1/3}\text{MnO}_3$  Films. *Adv. Mater.* **2014**, *26*, 2789–2793.
- (40) Ke, X.; Rzchowski, M. S.; Belenky, L. J.; Eom, C. B. Positive Exchange Bias in Ferromagnetic La 0.67 Sr 0.33 MnO 3/SrRuO 3 Bilayers. *Appl. Phys. Lett.* **2004**, *84*, 5458–5460.
- (41) Francis, A. J.; Cao, Y.; Salvador, P. A. Epitaxial Growth of Cu (100) and Pt (100) Thin Films on Perovskite Substrates. *Thin Solid Films* **2006**, *496*, 317–325.